Research Article

High-Resolution Strain Measurement for Biomechanical Parameters Assessment in Native and Decellularized Porcine Vessels

Juan Melchor [ID],[1,2,3] **Juan M. Soto** [ID],[4] **Elena López-Ruiz** [ID],[2,3,5] **Javier Suarez** [ID],[1] **Gema Jiménez** [ID],[2,3,6,7] **Cristina Antich**,[6,7] **Macarena Perán** [ID],[2,5] **Juan A. Marchal** [ID],[2,3,6,7] and **Guillermo Rus** [ID][1,2,3]

[1]*Department of Structural Mechanics, University of Granada, Granada 18071, Spain*
[2]*Instituto de Investigación Biosanitaria (ibs.GRANADA), Spain*
[3]*Excellence Research Unit "Modeling Nature" (MNat), University of Granada, 18071, Spain*
[4]*Department of Optics, Faculty of Physical Sciences, Complutense University of Madrid, Madrid 28040, Spain*
[5]*Department of Health Sciences, University of Jaén, Jaén, Spain*
[6]*Biopathology and Regenerative Medicine Institute (IBIMER), Centre for Biomedical Research, University of Granada, Granada, Spain*
[7]*Department of Human Anatomy and Embryology, Faculty of Medicine, University of Granada, Granada, Spain*

Correspondence should be addressed to Juan Melchor; jmelchor@ugr.es

Decellularized vascular scaffolds are promising materials for vessel replacements. However, despite the natural origin of decellularized vessels, issues such as biomechanical incompatibility, immunogenicity risks, and the hazards of thrombus formation still need to be addressed. In this study, we assess the mechanical properties of two groups of porcine carotid blood vessels: (i) native arteries and (ii) decellularized arteries. The biomechanical properties of both groups (n = 10, sample size of each group) are determined by conducting uniaxial and circumferential tensile tests by using an ad hoc and lab-made device comprising a peristaltic pump that controls the load applied to the sample. This load is regularly incremented (8 grams per cycle with a pause of 20 seconds after each step) while keeping the vessels continuously hydrated. The strain is measured by an image cross-correlation technique applied on a high-resolution video. The mechanical testing analyses of the arteries revealed significant differences in burst pressure between the native (1345.08±96.58 mbar) and decellularized (1067.79±112.13 mbar) groups. Moreover, decellularized samples show a significantly lower maximum load at failure (15.78±0.79 N) in comparison with native vessels (19.42±0.80 N). Finally, the average ultimate circumferential tensile also changes between native (3.71±0.37 MPa) and decellularized (2.93±0.18 MPa) groups. This technique is able to measure the strain in the regime of large displacements and enables high-resolution image of the local strains, thus providing a valuable tool for characterizing several biomechanical parameters of the vessels also applicable to other soft tissue presenting hyperelastic behaviours.

1. Introduction

Arterial graft remains the primary therapy for patients with advanced cardiovascular disease. The ongoing need for arterial conduits is due to the poor clinical efficacy of existing synthetic grafts in small diameter artery applications around (∼ 5 mm) [1, 2]. Besides, many patients with pathological arterial walls need an efficient replacement based on tissue engineering procedures [3–5]. In particular, tissue engineering has been successfully applied to fabrication of printed-based matrices for developing useful implants [6, 7].

The arterial graft typically involves a decellularization procedure depending on the geometrical shape and the biomechanical properties of the required tissue [8]. Moreover, the process of acquiring native arteries and their decellularization requires a difficult methodology, not always

put into practice in an optimum manner. In this study, we explore the possibility of obtaining porcine decellularizated arteries by applying an enzymatic digestion and detergent extraction procedure [1, 9, 10]. This process is able to provide implants to patients similarly to those made of synthetic materials, once the demanded biomechanical resistance is known. Some authors have also studied the fabrication of a hybrid tissue vascular graft by applying polymerized coatings on the outside of different aortic or carotid decellularized vessels, which significantly enhances their biomechanical behaviour [2, 11].

The outstanding role of assessing the biomechanical properties of biological specimens (in this case, different arteries) justifies the application of the mechanics of continuous media formalism. Particularly, it has been used to describe the results from several mechanical tensile tests aiming at retrieving the stiffness and elasticity of the samples. Typically, the mechanical characterization of the blood vessels has been obtained without taking into account the resolution of the displacements in axial or circumferential tests [12–14]. The error introduced by an inaccurate distance measurement is translated into significant misleading variations of the mechanical parameters. In this regard, we propose an image cross-correlation algorithm to improve the strain tracking experienced by the sample during the stress tests, thereby providing a high-resolution characterization of their mechanical parameters. The researchers that may introduce these mechanical concepts in the field of tissue engineering or clinical practice need this accurate characterization of the mechanical properties [15–17].

Soft tissues (such as blood vessels), understood as hyperelastic materials when subjected to uniaxial loads, are characterized by relevant shape changes as well as a strongly nonlinear response. Hyperelastic materials experience a great strain when a load is applied. Nevertheless, once the load is removed they return to a position very close to the initial one. On the other hand, when cyclical loads are applied to these materials, a considerable dissipation in the energy is exhibited as a response to the stress. The realization of this work has been based on the functions of the deformation energy suitable for soft tissues study developed by Holzapfel, Ogden, and Vito [18–21]. In this way, a semianalytical description of constitutive equations for soft tissues is explored and then it has been applied to develop a new technique for measuring the strain in mechanical tensile tests.

The remainder of the paper is organized as follows. Section 2 briefly describes the mechanical behaviour of the artery along with the derivation of its stress tensor. Next, Section 3 is devoted to the strain tensor. Then, Section 4 includes the experimental setup, the preparation of the biological samples, and the details of the statistical analysis performed in the experiment. Later, Section 5 describes the image cross-correlation algorithm proposed in this work for a better characterization of the sample mechanical properties. The following section includes the results from the mechanical tests along with the histological comparisons between native and decellularized vessels. Finally, Section 7 summarizes the main conclusions of the study and paves the way for future work.

2. Biomechanical Stress Tensor on Arteries Samples

The methodology applied for the mechanical characterization is based on the stress-strain curve analysis of the sample tested until failure. As later explained in Section 4.1, this curve is obtained by applying a loading stress to the sample and recording a process by a camera, therefore obtaining a 2D image for each load value applied to the specimen. For this purpose, Cauchy stress has been considered the most appropriate since it corresponds to the force or load divided by the area of the section of the sample as follows:

$$\sigma = \frac{N}{A}, \tag{1}$$

where σ is known as Cauchy stress, N is the applied force (in our experiments it corresponds to the load applied to the blood vessel in each measurement), and A is the area of the sample section. Consequently, σ is calculated by taken into consideration the geometry of the sample.

In particular, the porcine vessels exhibit the strain-stress curve displayed in Figure 1. In this representation, two different behaviour phases can occur depending on the amount of strain experimented by the sample, as explained in [22, 23]. Firstly, for low values of the strain a linear region exists in which the elastin composition prevails in the mechanical response of behaviour of the artery which is the collagen composition. By linear fitting of each region it is possible to obtain the value of Young's modulus that characterizes the elastin and collagen phases, respectively. Collagen Young's modulus is much larger than its elastin counterpart, thus implying a lower stiffness of the sample in this phase. Therefore, the collagen phase is chosen because in the elastin phase there are not enough significant points to approximate with reliably. Besides, this elastin phase is considered when the sample has less rigidity and the hyperelastic model is better fit with collagen region.

Moreover, it is also important to obtain the strength of the material (F_m) as the maximum load to failure, so that if the loading stress continues then the material breaks. Other relevant parameters are the ultimate tensile strength (UTS) defined as $S_r = F_m$ and the elongation under maximum load, as explained later. Furthermore, the true (or logarithmic) deformation $d\varepsilon$ is defined as the ratio between the increase in length ($\triangle l$) and the length of the sample (l) at any instant,

$$d\varepsilon = \frac{\triangle l}{l}, \tag{2}$$

The values of engineering ($d\varepsilon$) and logarithmic (s) deformations are related according to the following expression:

$$s = \ln\left(1 + \frac{\triangle l}{l_0}\right), \tag{3}$$

From the values (F, $\triangle l$) obtained in the mechanical test, one is able to plot the uniaxial component of tensors of Cauchy (σ) and the finite strain tensors (s) as displayed in Figure 1, thus obtaining its characteristic points (basically, the point in which the material suffers the mechanical failure and the point of the transition between elastin and collagen regions).
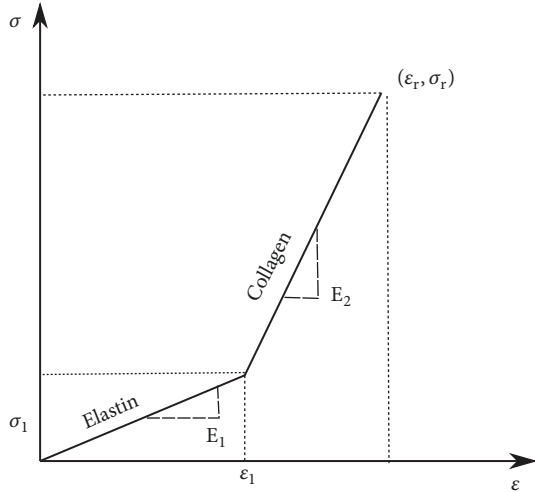
FIGURE 1: Theoretical stress-strain relationship for an elastic swine vessel reported by Garcia Herrera [22, 23]. Different Young's modulus values, E_1 and E_2, characterize the regions in which the mechanical behaviour is dominated by elastin and collagen composition of the vessel, respectively. These regions are separated by a critical point of the curve of stress-strain $(\varepsilon_1, \sigma_1)$ and the collagen phase ends abruptly when the failure of the material occurs $(\varepsilon_r, \sigma_r)$.

3. Biomechanical Strain Tensor Calculation on Arteries Samples

From the previous section we have derived an expression for the Cauchy stress that depends on the strain tensor. Let us now define two Cartesian directions, a and b (in our case the plane defined by ab corresponds to the XY plane, since the 2D image is recorded in the plane parallel to the force applied to the specimen). The plane ab is discretized by defining a 2D mesh within a region of interest (ROI, denoted as x) distributed along the aforementioned directions. Then, both the deformation gradient (F) and the Green-Lagrange axial deformation (S) are obtained to estimate the deformation of the specimen.

First, the deformation gradient of the region of interest in the direction a regarding the address b is a tensor given by

$$F_{ab} = \frac{\partial x_a}{\partial x_b^0}, \tag{4}$$

where in the previous expression the superscript 0 refers to the position at the initial instant of the experiment. F_{ab} is a Jacobian matrix or deformation gradient that acts as an operator transforming certain initial vectors (belonging to the environment of a point) from a reference configuration into the corresponding vectors in a final configuration. In this case, the initial state is when any deformation is applied to the sample whereas the ending state is measured after several successive deformations even leading to the failure of the material.

For the computational calculation, (4) must be discretized but this procedure is nontrivial. Since we move in a 2D plane,

one can define the four components in which Lagrangian notation is applied as

$$F_{11}^k (i, j) \approx \frac{x_1^k (i, j) - x_1^k (i, j + 1)}{x_1^0 (i, j) - x_1^0 (i, j + 1)}, \tag{5}$$

$$F_{12}^k (i, j) \approx \frac{x_1^k (i, j) - x_1^k (i, j + 1)}{x_2^0 (i + 1, j) - x_2^0 (i + 1, j)}, \tag{6}$$

$$F_{21}^k (i, j) \approx \frac{x_2^k (i, j) - x_2^k (i, j + 1)}{x_1^0 (i, j) - x_1^0 (i, j + 1)}, \tag{7}$$

$$F_{22}^k (i, j) \approx \frac{x_2^k (i, j) - x_2^k (i + 1, j)}{x_2^0 (i, j) - x_2^0 (i + 1, j)}, \tag{8}$$

with i and j being the original coordinates representing the recorded ROI of the specimen (therefore, it is an immobile reference) and the superscript k denotes the video frame of the sequence of the experiment (k = 0 is the initial frame) since the stress σ is evaluated for each load increment in the tensile test. On the other hand, subscripts 1 and 2 denote, respectively, the X and Y Cartesian directions to which the deformation of the analyzed ROI points. Note that in this formulation the initial position of the specimen (superscript 0) has been defined as reference. These expressions justify the need for the application of an interpolation between frames k to facilitate the convergence. Note also that if the denominator reaches an extremely low value, then the value of F would be too large. To avoid this, the amount of load applied between consecutive video frames must be appropriate for linearly fitting the strain (and the deformation tensor components). Once the deformation gradient is computed, then Green-Lagrange strain can be derived as

$$\varepsilon = \frac{1}{2} \left(FF^T - I \right) \tag{9}$$

in which I denotes the identity matrix and T superscript is the transposed matrix. Physically, the strain ε represents the quadratic difference between the lengths of deformed and nondeformed state; that is to say, this tensor measures the difference between the squares of differential surface elements in both cases.

By considering that our interest lies in the deformation in the direction in which the load is applied to the sample, then (9) is simplified to

$$e = \frac{\triangle l}{l_0} = \frac{1 - l_0}{l_0}, \tag{10}$$

where e is the elongation at maximum load. For the particular case of a vessel sample let us assume that it has a thin wall; namely, its thickness is lower than one tenth of its length (see [24]). This approximation allows for the treatment of the wall as a surface and is subsequently using the Laplace-Young equation to estimate the circumferential stress created by an

internal pressure (burst pressure) in a thin-walled cylindrical pressure vessel as shown below

$$T_c = \frac{Pr}{t} \longrightarrow$$
$$P = \frac{2tT_c}{r},$$

(11)

where $T_c = N/A$ is the circumferential stress, P is the pressure, r is the radius, and t is the sample thickness. Note that double the thickness has been considered in (11) due to the form of adjusting the sample (ring) to the clamps, as further explained in Section 6.2.

4. Materials and Methods

4.1. Mechanical Testing. The theory of large strains has been applied for studying carotid vessels of swines as hyperelastic materials, in order to test their tensile strength and elongation at fracture. The samples have been grouped into two groups, native and decellularized arteries, further referred to as NA and DA, respectively. The main objective of this study is evaluating the impact of the arteries decellularization procedure on their mechanical properties. In particular, this analysis requires the following:

(1) Stress rupture testing of each type of artery by calculating the maximum tensile load required for the fracture.

(2) Computing the modulus of elasticity NA and DA vessels.

(3) Extracting the hydrostatic pressure from arteries under circumferential tension.

(4) Analyzing the relationship between the mechanical properties and histological analyses of vessels.

To carry out these goals, the strain-stress curve of each sample needs to be measured. With this purpose, the tensile-compression press included in Figure 2 has been arranged for the mechanical test of the samples. In particular, it includes the bars that support the entire setup, a water container to apply a load to the vessel and another bucket filled with water acting as a counterweight. The press, as indicated in Figures 2 and 3(a), consists of two clamps fabricated in epoxy resin for favoring the fastening of the arteries. The vessel sample remains fixed by means of PLA-printed holders (see Figure 3(b)) that prevent the artery from torsion and other undesired movement.

A peristaltic pump (controlled by an Arduino microcontroller) is used to increase the load gradually at 8 grams increments, while keeping the vessels continuously hydrated. After each load step, a pause of 20 seconds has been set in order to stabilize the system and avoid undesired rheological phenomena or oscillations that may hinder the tracking. It is worth pointing out that such a small load increment has been chosen because when the motion between consecutive frames is excessively large, a nonlinear regime of movement may occur.

Then, the deformation has been measured by recording a high-resolution video and obtaining the displacements from the recorded images as previously reported [2, 25, 26]. In particular, we apply a cross-correlation image algorithm that is described thoroughly in Section 5 for strain measurement. This video is triggered at the beginning of pumping and custom image capture software is used to record at a rate of 1 frame per load increment until the sample breakdown. A conventional camera (IPEVO Ziggi-HD High Definition USB CDVU-04IP model, 5 Mpix, 1280×720 resolution) has been used to acquire the image sequence in the parallel plane with respect to the surface in which the deformation tensor is measured. Finally, it is worth underlining that the preparation of the experiment is essential and includes some basic steps:

(i) By engraving the vessel with a speckle or random dot pattern the monitorization of the strain of different regions of the sample is facilitated. Taking into account the fact that the strain is measured by using a cross-correlation technique (as explained in Section 5), if more details are added to the vessel then this algorithm works better as more characteristic points can be followed with the tracking procedure. The analysis of an image sequence based on correlation works better if some details of the sample changes during the experiment, as this operation highlights the morphological differences that have occurred. As the surface of the sample is flat and without any striking feature, the staining is mandatory if a reliable strain assessment is needed. In this case, acrylic black paint has been used to apply the pattern over the sample and then the sample is dried out a few minutes.

(ii) A uniform background and illumination throughout the entire experiment help to maintain an optimum contrast in the recorded image

(iii) The arteries must be kept continuously hydrated to maintain their mechanical properties, for instance, by spraying them with PBS during the mechanical test. Thanks to the waterproof capability of the acrylic paint, once the artery is stained the pattern is not removed with the PBS, thus providing an enduring marking of the sample.

(iv) All the blood vessels are cut with the same mold (see Figure 3(c)) for tailoring them and maintain similar dimensions, thus controlling the area of the minimum section where each one break.

4.2. Tissue Harvest and Preparation. Porcine carotid arteries are obtained from a slaughterhouse and transported to the laboratory stored in cold PBS with 1% penicillin/streptomycin. Immediately after arrival, carotid arteries are cleaned to remove the excess of connective and adventitial tissues. Next, the carotid arteries are rinsed in sterile PBS and cut into segments of 3-5 cm in length and 3-4 mm in diameter. Finally, they were immediately frozen in PBS at -80˚C for later use; it has been previously shown that the freeze-and-defrost process does not significantly affect artery mechanics [26–28]. At the time of testing, specimens were
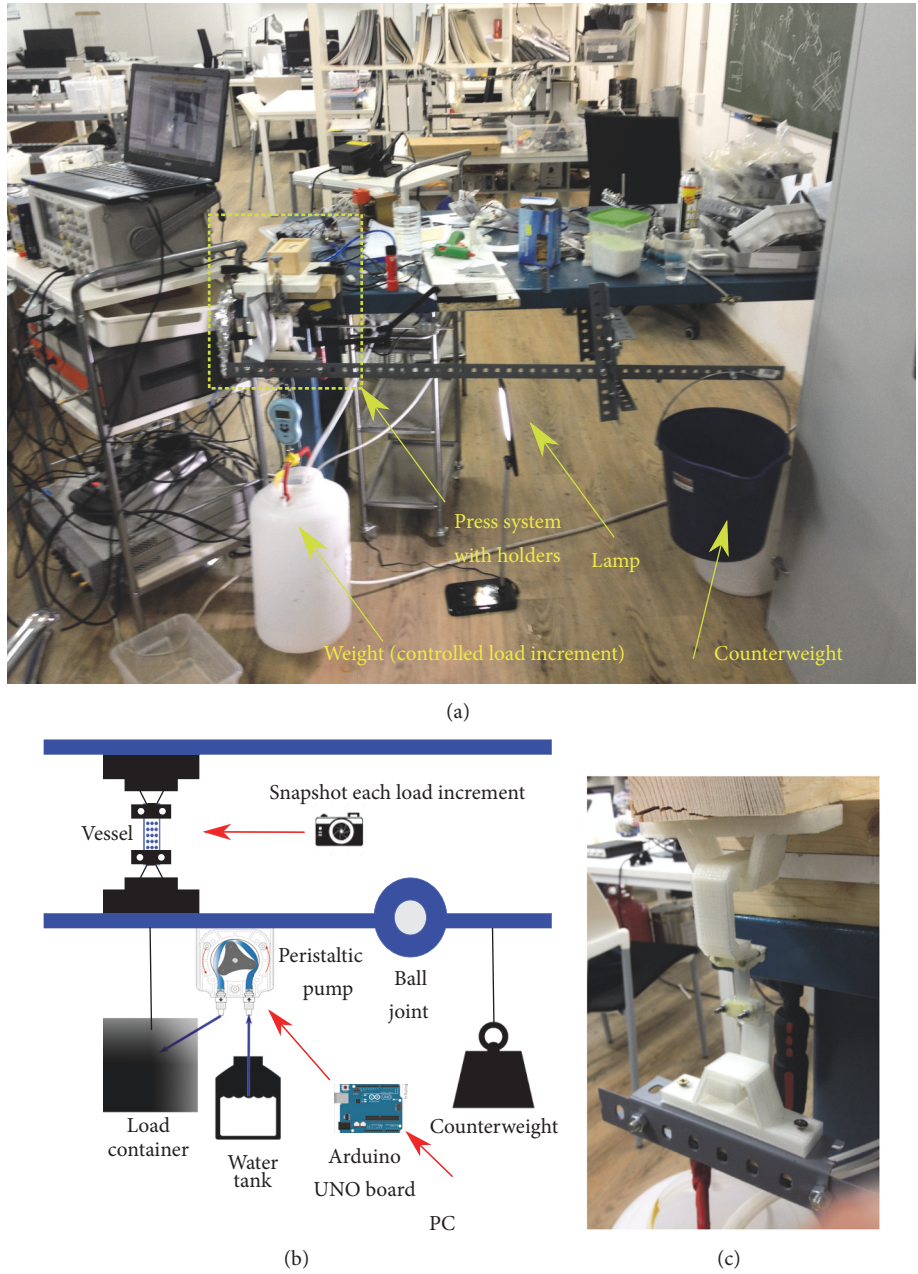
(a)

(b)

(c)

FIGURE 2: (a) Press setup comprising clips and fasteners for holding the sample attached to several weights and counterweights for controlling the applied load. The data are sent to a computer and processed with MATLAB. (b) Schematic representation of the whole measurement system. The artery suffers an increasing load and the process is registered by a camera. (c) Placement of the sample into the clamps to undertake the uniaxial tensile experiment.

thawed in a 37°C water bath and tested within 1 h of thawing [29].

4.3. Decellularization Process.
The decellularization process of carotid tissue samples is performed as previously described [2] using enzymatic digestion and detergent extraction. Carotid arteries were immersed in deionized water for 24 h at 4°C followed by treatment with 0.05% Trypsin with 0.02% EDTA (Sigma Aldrich, St. Louis, MO, USA) for 1 h at 37°C. After a short rinse in PBS to remove trypsin excess,

the samples are treated with a solution of 2% Triton X-100 and 0.8% ammonium hydroxide (Sigma) in deionized water for 72 h at 4°C. This solution has been changed every 24 h. After the decellularization, samples were washed in deionized water three times, for 24 h each, to remove chemical residues. All these steps of the preparation are carried out under continuous shaking except trypsin incubation.

4.4. Histological and Immunofluorescence Analyses.
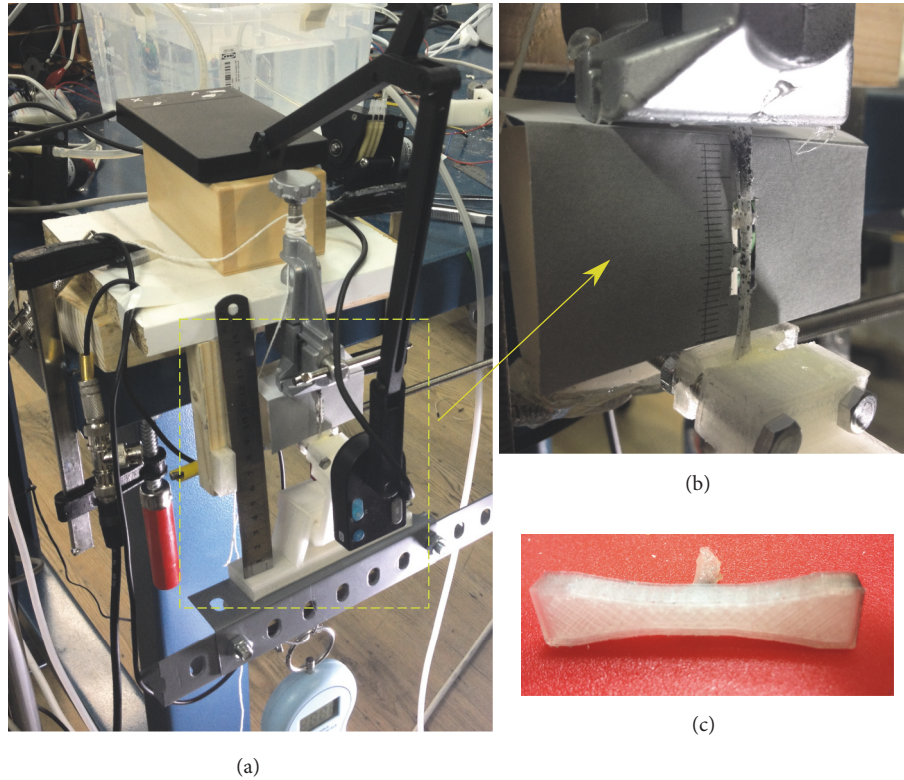Samples were fixed in 4% paraformaldehyde, embedded in paraffin in

FIGURE 3: (a) Close-up view of the camera attached to the press setup for performing the tracking of the motion. (b) Vessel sample placed in the press during a test. Note that a random speckle pattern has been impressed over it to ease the strain tracking with the image cross-correlation algorithm. (c) Mold printed in 3D with polylactic acid (PLA) to maintain the dimensions of the samples.

an automatic tissue processor (TP1020, Leica, Germany), cut into 5 mm sections, and stained with Hematoxylin and Eosin (H&E) and Masson's Trichrome as previously reported [30]. Images are acquired with an inverted microscope (Nikon H550s, USA).

4.5. Scanning Electron Microscopy (SEM). Arteries are washed twice with 0.1 M cacodylate buffer (Sigma) and fixed with 2.5% (w/v) glutaraldehyde in 0.1 M cacodylate buffer (pH 7.4; Poly-sciences, Warrington, PA) for 4 h at 4°C. Thereafter, samples are rinsed several times with sodium cacodylate buffer. After fixation, samples are postfixed with 1% w/v osmium tetroxide for 1 h RT, dehydrated stepwise with ethanol (50%, 70%, 90% and 100%, 15 min each), critical point dried in CO_2, and gold coated by sputtering. Finally, the images are examined by using a FEI Quanta 400 scanning electron microscope (Oregon, USA).

4.6. Statistical Analysis. Each experiment has been conducted with 10 samples. Results are presented as mean ± standard deviation (SD). A Student's t-test is used to test the significance level between specific cases. The results are considered significantly different at p-values $p < 0.05(*)$ and $p < 0.01(**)$.

5. Image Cross-Correlation Algorithm for Strain Tracking

Traditionally, obtaining precise strain measurements during uniaxial tensile testing can be performed by clamping a strain gauge to the sample. Nevertheless, here we aim at obtaining a contactless strain measurement, whereby we need laser extensometers or a recording of digital images series and then applying a digital image correlation software; see [31, 32]. The most conventional correlation algorithms monitor the positions of two parallel markers during the experiment (for instance, comparing an intensity profile along the tensile direction), and hence the strain of the sample can be calculated. According to previous works [32], one of the main difficulties for strain assessment based on correlation occurs when the deformed area of the sample is large to hinder the matching of consecutive images. In this regard, our protocol of measurement is robust thanks to the speckle engraving of the sample.

As previously explained in Section 4.1 and sketched in Figure 2(b), a press system has been designed for conducting different mechanical test over the vessel samples. Note that it is important to choose an appropriate distance for recording so that the failure of the sample occurs far from the edges of the image and at the same time make the most of the camera field of view. Moreover, for obtaining a good calibration for

k=1

stack N images

RGB to gray

ROI selection

Discretized ROI

Image cross-correlation: alignment

for k=1:(N-1)

A

k

B

k+1

2D movement matrix between images A and B

average

ε_k

k=k+1

NO

k=N?

YES

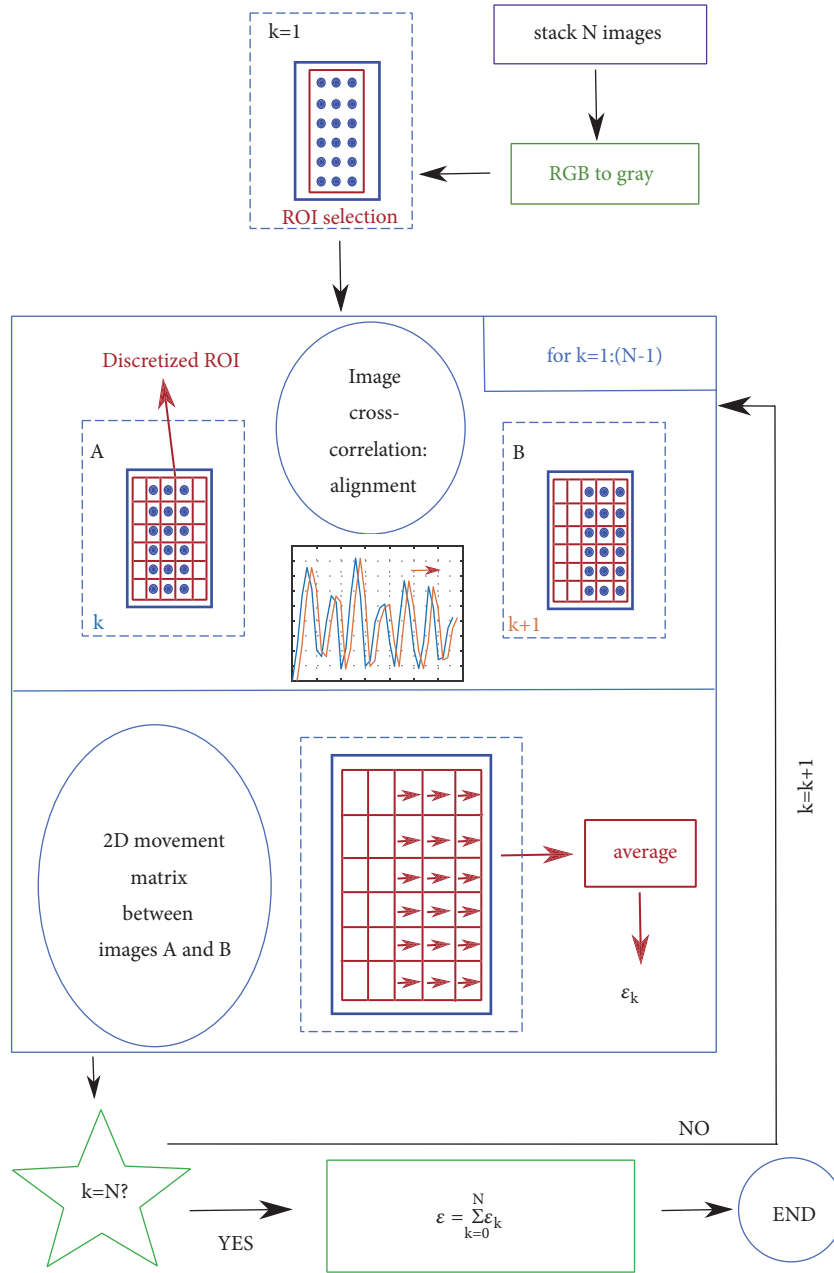$$\varepsilon = \sum_{k=0}^{N} \varepsilon_k$$

END

FIGURE 4: Flowchart summarizing the algorithm of cross-correlation for finding the strain from an image sequence.

the measurement of the strains, the pixel size of the camera and its resolution must be taken into account or, alternatively, an object of known dimensions can be included in the recorded field of view. In this way, it is possible to correlate the measurement in pixels registered by the camera and the real distances. After the acquisition of this image sequence, a tracking algorithm based on image cross-correlation is applied sequentially between each consecutive pair of frames of the sequence. This algorithm, also summarized in the flowchart from the Figure 4, follows these steps:

(1) We start with a sequence of N input images that contains a recording of all the experiment. If they are in RGB color (as in our case), they are firstly converted to grayscale.

(2) A ROI or mask is defined in the first frame of the sequence so that all the images outside this mask are ignored. Typically, this ROI is the middle area of the vessel in order to circumvent unwanted border effects. For this ROI the movement is approximated by a piecewise linear function.

(3) A discretization is applied to transform the ROI into an array of discrete blocks, so that the number of characteristic points is reduced. The tracking algorithm is applied to each of these blocks instead of applying it

pixel by pixel, for alleviating its computational cost. Note that the number of blocks should be optimized by taking into account both the camera resolution and the amount of strain experienced by the sample. For instance, if the block-size is extremely small then the ROI will contain too many blocks, thus producing an increase in computation time. Moreover, these tiny blocks are more prone to noise problems. Conversely, the discretization with a small number of large blocks is expected to hinder the most subtle movements. Furthermore, the largest the strain is experienced by the sample, the more the blocks are needed to monitor the process while minimizing in the measured distances. Consequently, there is a trade-off between the computational cost and the precision of the tracking algorithm. In this case, a rectangular discretization mesh has been chosen with blocks of 8 pixels in width by 16 pixels in height.

(4) Between each pair of consecutive frames, hereinafter referred to as A (the first image) and B (the second one), the motion of each block of the discretized ROI is measured by finding the peak of cross-correlation between A and B. We compute the maximum of image cross-correlation (xcorr) to obtain the motion (strain) that have occurred within every discretization block of the block between A and B. One can obtain the 2D strain as follows:

$$\varepsilon\left(x^{k}_{1}, x^{k}_{2}\right) = \max\left[\text{xcorr}\left(\text{image}_{k}, \text{image}_{k+1}\right)\right] \quad (12)$$

In this way, the best matching between the two images is found. It is important to highlight that, as the images are bidimensional (2D), the correlation is also evaluated in the 2D plane. It is worth remarking that the speckle pattern impressed in the artery helps out with tracking as it enhances the number of features to be trailed unless an undesired torsion movement occurs. Nevertheless, the two clamps that hold the sample edges prevent this torsion from happening.

(5) Taking into consideration the fact that throughout our experiments only uniaxial tests (e.g., along x_1 axis) have been performed, then the strain in that direction prevails over the torsion movement (along x_2 axis). Consequently, by averaging the 2D motion of all the blocks one obtains the mean strain suffered by the sample under test for the k-image of the sequence, denoted as

$$\varepsilon_{k} = \text{mean}\left[\varepsilon\left(x^{k}_{1}, x^{k}_{2}\right)\right]. \quad (13)$$

(6) Now we proceed with the following pair of images of the sequence. The initial ROI is updated for taking into account the mean movement (ε_k) experienced by the sample in the previous pair of frames. The steps ((3)-(5)) are repeated until reaching the end of the recorded sequence.
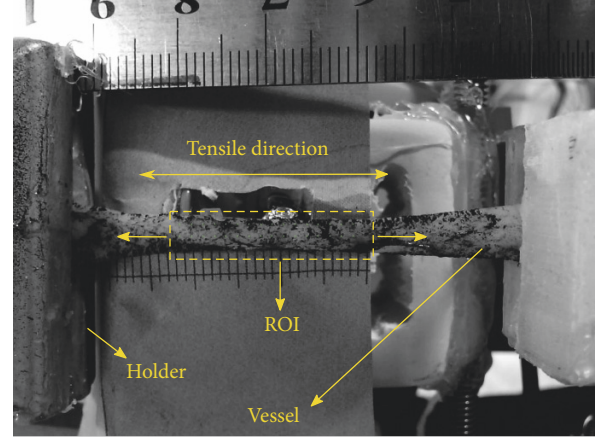

FIGURE 5: Example of vessel attached to two holders that secure it during the uniaxial tensile experiment, thus avoiding undesired torsion movement. The region of interest (ROI) has been delimited by a dashed yellow line.

(7) We compute the global strain along all the experiment by adding all the strain between consecutive images:

$$\varepsilon = \sum_{K=1}^{N-1} \varepsilon_{k} \quad (14)$$

Thanks to this image correlation algorithm different mechanical tests have been conducted and monitored, namely, uniaxial test (explained in Section 6.1) and circumferential tensile stress test (Section 6.2).

6. Results and Discussion

6.1. Uniaxial Testing. For uniaxial testing, the sample is placed as shown in Figure 5 and stretched with the experimental setup from Figure 2. From this framework it is possible to obtain a 2D strain, but the movement along the direction in which the load is applied has a prevailing effect (as demonstrated in the experiment sequences displayed in Figures 6 and 7). Consequently, only this direction is considered for the analysis. In this way, the strain-stress curve of the samples is obtained (see an example for two arteries, one of each group, in Figure 8(a)). Next, Young's modulus has been extracted as the slope of its linear region (see Figure 8(b)). We recall that this linear region is associated with the collagen content of the sample. In particular, from Figure 8(a) the expected value for Young's modulus is 4.31±0.25 MPa for the decellularized sample and 3.11±0.15 MPa for the native one. After computing this stress-strain curve for n = 10 samples in each category, we obtain the results included in Figure 8(b): 4.98±0.67 MPa for the decellularized versus 3.53±0.56 MPa for the native specimens. These values are in good agreement with the usual blood vessels range of Young's modulus [10, 13, 26]. The value of Young' modulus slightly changes when a conventional correlation algorithm based on the tracking of two parallel markers is used. These markers are placed in both edges of the vessel along the direction in

(a) Load = 44.748 g

(b) Load = 180.510 g

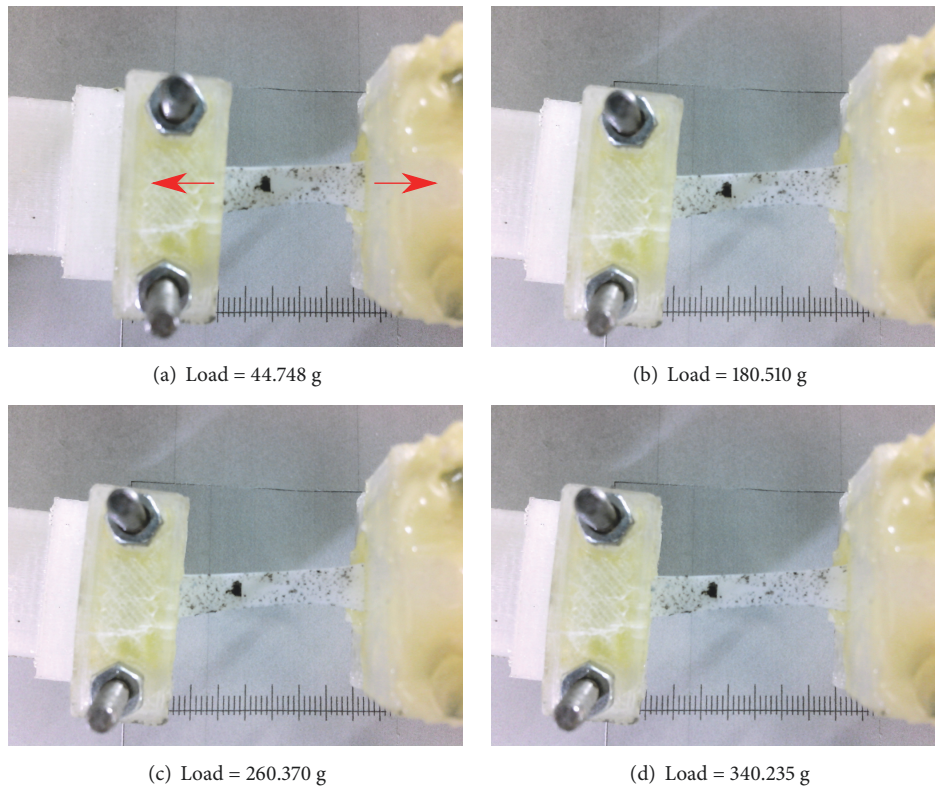(c) Load = 260.370 g

(d) Load = 340.235 g

FIGURE 6: Four different frames from a recording of a uniaxial tensile test in a decellularized vessel with an increasing load. The sample is stretched in the direction marked with red arrows, and the strain tracking is enhanced thanks to the speckle pattern applied to the sample.
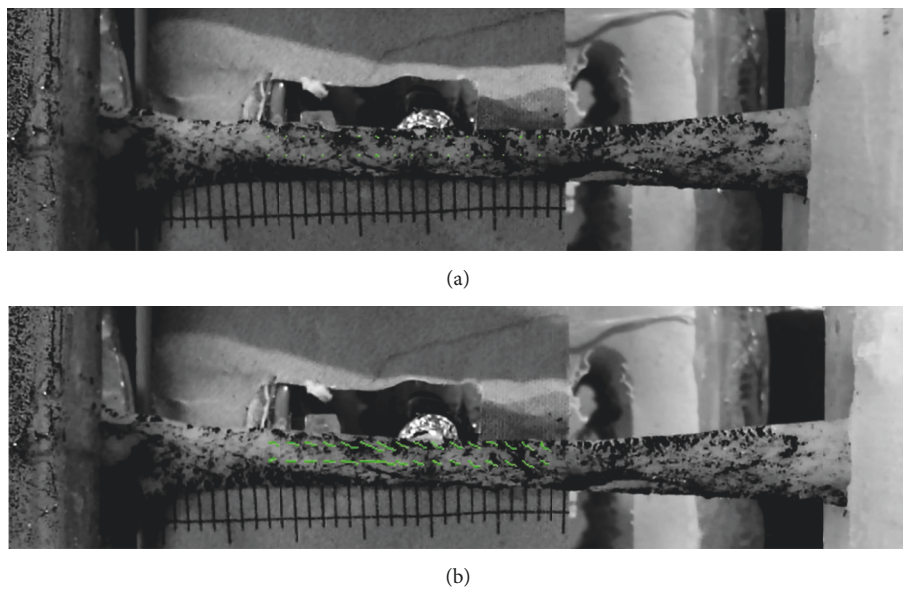

(a)

(b)

FIGURE 7: Two different frames showing the typical output of the tracking algorithm for uniaxial tensile test over an artery. Green dots represent the center of each block in the discretized ROI and the green line represents the movement in regard to the first frame of the recorded sequence. The reader is further referred to the video Visualization 1 in Supplementary Materials to see the whole tracking sequence.
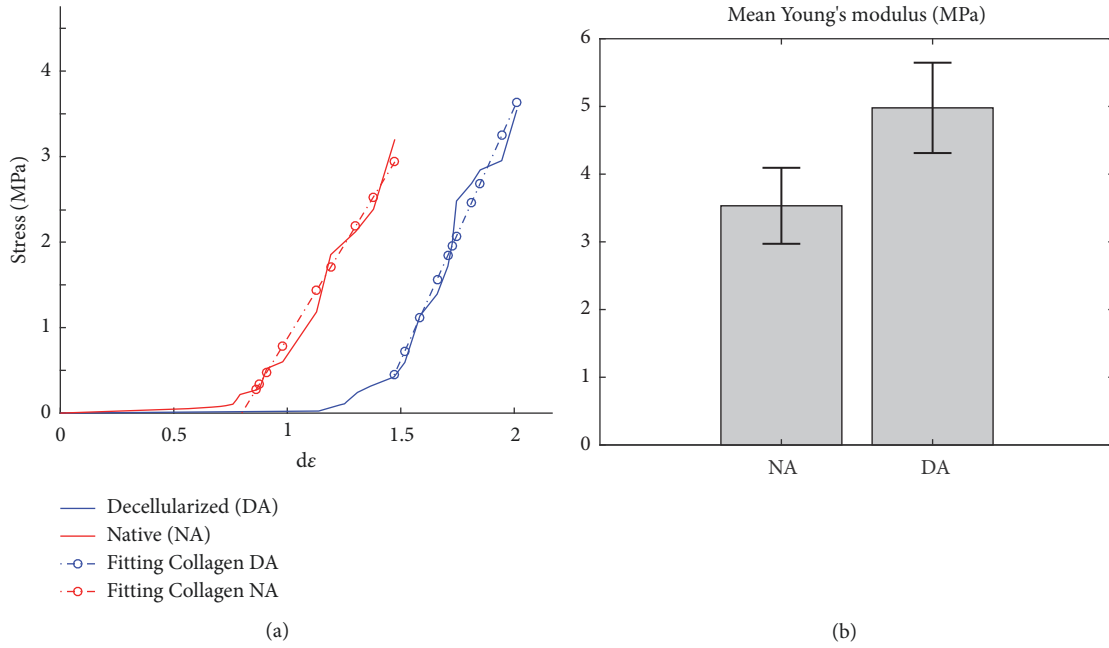
FIGURE 8: (a) Experimental stress-strain relationship for elastic swine vessels, along with the linear fitting of the curve along the collagen region. (b) Young modulus for each group of vessels (represented as mean+-SD, (**) p < 0.01).

which the load is applied. With this procedure one reaches a value of 4.47±0.82 MPa for decellularized and 3.46 ±0.75 for native vessels, respectively. The underestimation of Young's modulus is probably due to the deformation experienced by the sample, hence obstructing the tracking of the strain. The artery warped not only along the longitudinal direction, as expected in a uniaxial test, but also in the traverse direction. Moreover, by averaging several 2D blocks of the sample instead of only using 1D intensity profile correlation-based matching we obtain a more accurate measurement, as the small undesired and unavoidable torsion of the sample along the traverse direction has also been taken into account. The deformation maps have been also analyzed for native and decellularized arteries at several elongation ratios (see Figure 9). An initial cross-section of 20 mm × 5 mm has been considered for all the vessels.

Indeed, there exist relevant changes (p-values of p < 0.01 in Student's T- test) between both groups. Therefore, it could be interpreted as the procedure of decellularization has a remarkable impact on elasticity.

6.2. Ring Testing. Ultimate tensile strength, maximum load and burst pressure has been determined for ring sections of arteries (n = 10 samples in each group), in order to test the circumferential stress. The ring sections are prepared as explained in Section 4.2 and mounted on custom-made holders. Each sample is tested by applying an increasing load until failure. The diameter, width, thickness, and length of each sample used for the calculations aforementioned in Section 2 are measured with a high-precision slide caliper. The sample displacement is determined by the image correlation algorithm and, in this case, the speckle pattern is

engraved in the transverse wall of the ring. We must underline that the mean radius of the ring samples has been used for calculations because it represents the distance to the neutral axis or centroid.

The burst pressure of the samples is calculated from their maximum load to failure. We recall that twice the sample thickness has been considered as defined in (11). The ring is arranged wrapping the two clamps and is stretched along a certain direction in which there is a double layer of vessel; thus the effective thickness is twice that of the ring. The radial stress is calculated and converted to millibars by considering the load, the mean radius and the circumferential UTS [9, 24, 33]. In comparison with the uniaxial test, the circumferential mechanical properties are significantly different due to different disposal of vessel fibers along longitudinal and circumferential directions.

The mechanical testing revealed significant differences between NA and DA rings. As summarized in Figure 10, there exist relevant dissimilarities between the mean burst pressure of the native arteries (1345.08±96.58 mbar) and the decellularized group (1067.79±112.13 mbar). Furthermore, there also exist differences regarding the maximum load that each type of artery can stand: the native stands 19.42±0.80 N whereas the decellularized is able to withstand a lower value (15.78±0.79 N). Finally, the circumferential UTS is also different, with an expected value of 3.71±0.37 [MPa] within the native group while in the decellularized this value decreases (2.93±0.18 [MPa]).

6.3. Histological Characterization of Native and Decellularized Arteries. As explained in Section 4.2, the samples are first

(a) Native arteries

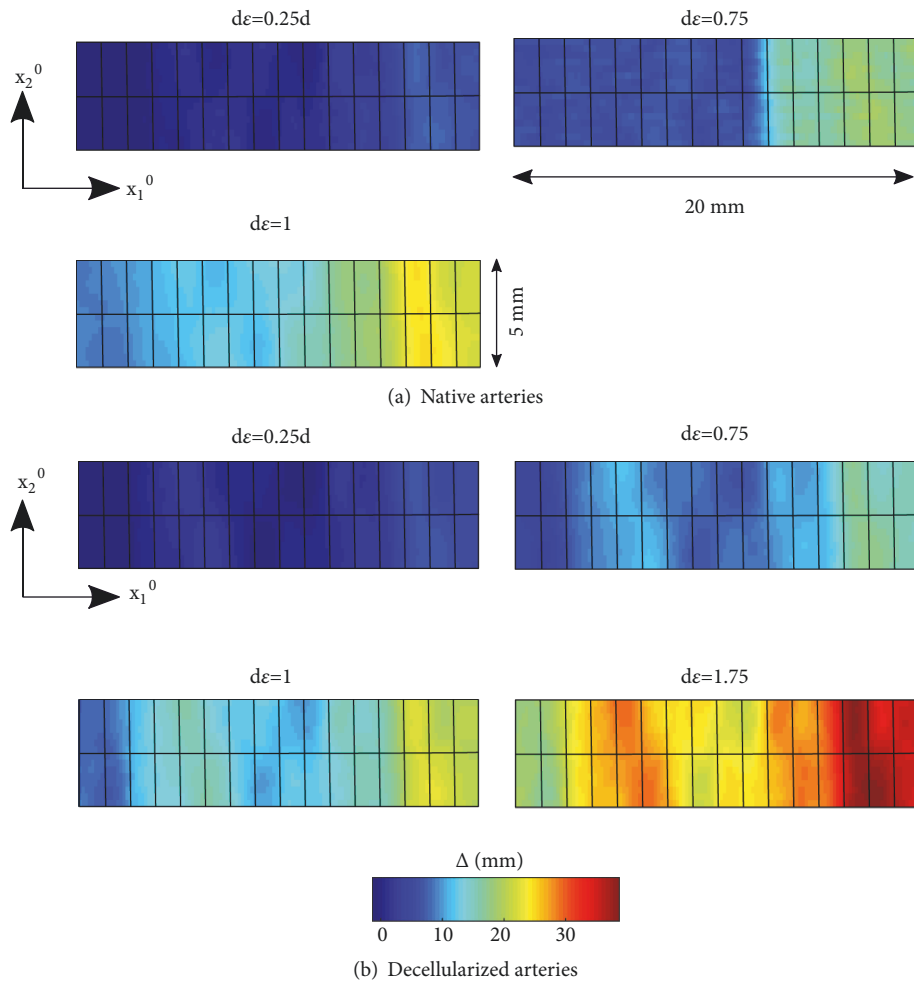

Δ (mm)

(b) Decellularized arteries

Figure 9: Deformation maps for a native (a) and decellularized (b) vessel, evaluated at different elongation ratios. An initial rectangular cross-section of 20 mm × 5 mm has been considered in all cases. The rectangular grid accounts for the discretization mesh applied for the tracking algorithm.

(a) Maximum load (N)

(b) Ultimate tensile strength (MPa)
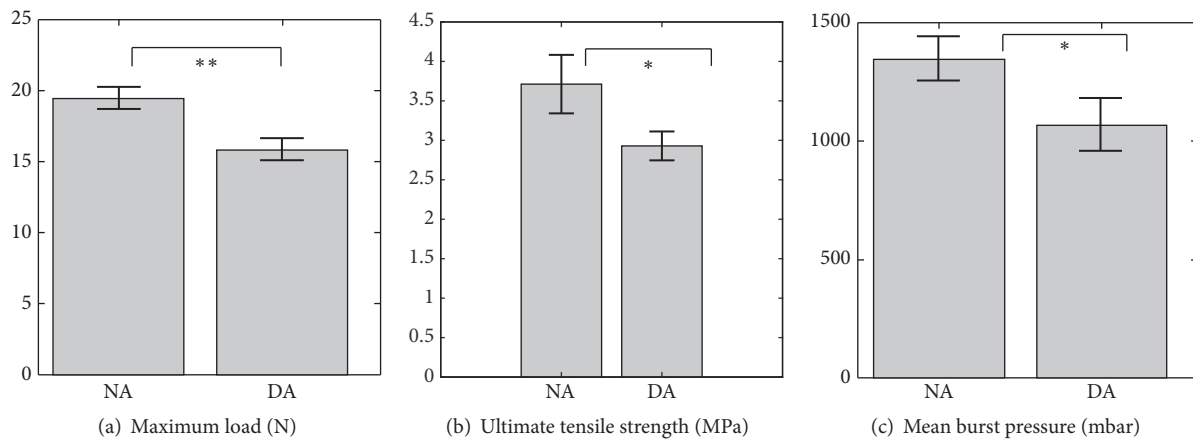
(c) Mean burst pressure (mbar)

Figure 10: Comparison between the mechanical parameters of native (NA) and decellularized (DA) arteries in the circumferential stress test, including the load (a), ultimate tensile strength (b), and hydrostatic burst pressure (c) from annular portions (rings) of samples. All the results are represented as mean+-SD, (∗) $p < 0.05$ and (∗∗) $p < 0.01$.
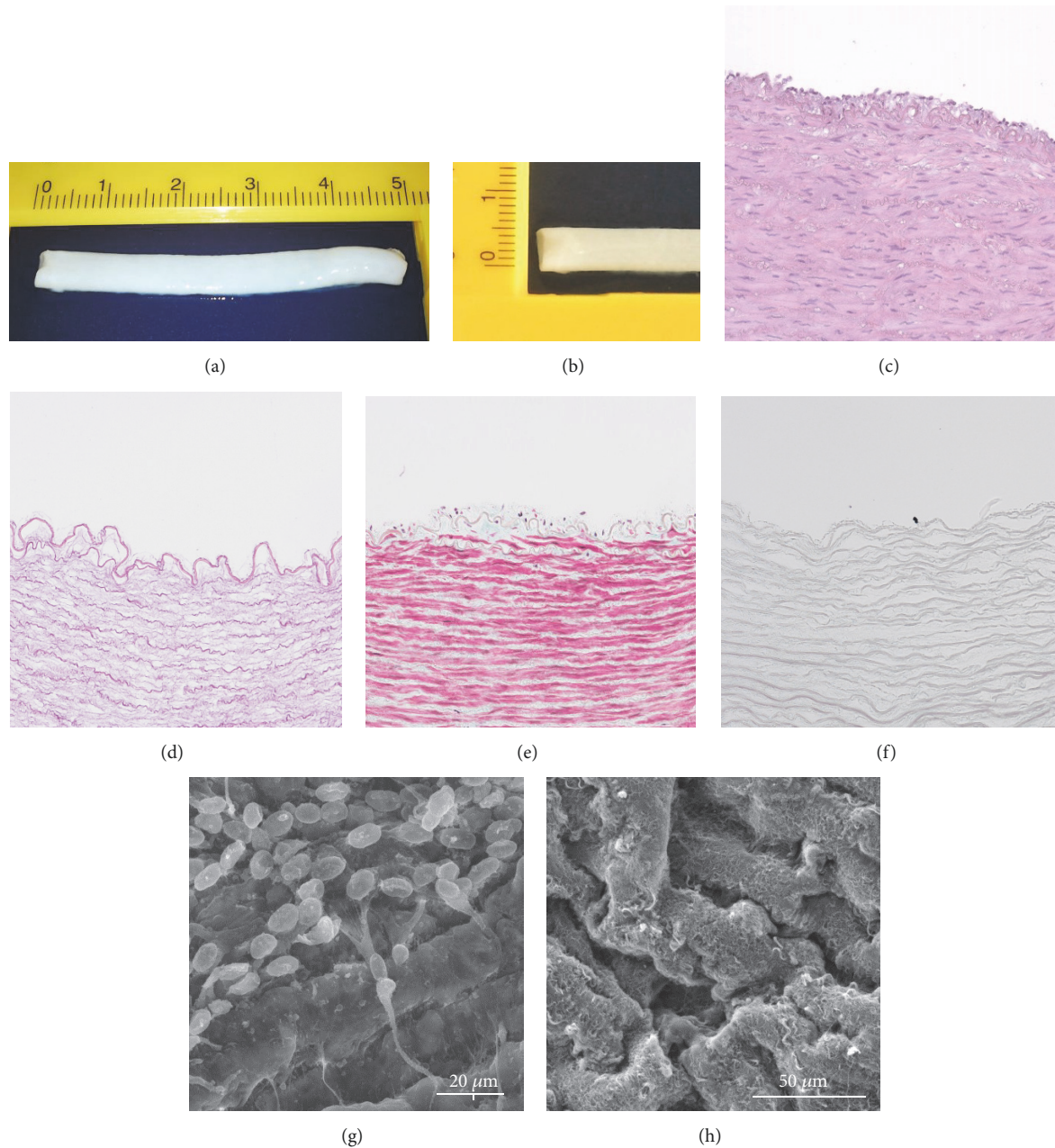
(a)

(b)

(c)

(d)

(e)

(f)

(g)

(h)

FIGURE 11: Characterization of porcine carotid arterial tissue before and after decellularization. (a,b) Macroscopic images of decellularized left common porcine carotid artery (artery length ~ 50 mm; inner diameter ~ 4 mm). Histology of porcine arteries: (c, e) native arteries and (d, f) decellularized arteries. (c) H&E staining of native arteries. (d) H&E staining of decellularized arteries showing complete removal of vascular cells. (e) Masson's Trichrome staining of native arteries. (f) Masson's Trichrome staining of decellularized artery showing collagens fibers and no cells (20x magnification). SEM micrographs of the luminal surface: (g) native arteries and (h) decellularized arteries; scale bar indicates 20 μm and 50 μm, respectively.

prepared and cut (see Figures 11(a) and 11(b)). Then, histological analyses and scanning electron microscopy (SEM) are performed on artery samples to demonstrate the efficacy of the decellularization process in native carotid arteries. Complete removal of vascular cells is confirmed by H&E and Masson's Trichrome staining after the decellularization procedure (Figures 11(d) and 11(f)) when compared with native arteries (Figures 11(c) and 11(e)). Native arteries showed

high density of cells embedded in collagen fibers (stained turquoise) (Figure 11(e)), while no cells were detected in the decellularized arteries (Figures 11(d) and 11(f)). In addition, the characteristic concentric layers of elastin (stained pink) and collagen fibers of native arteries remained intact at decellularized arteries showing the same circumferential orientation and a well preserved ECM (Figures 11(d) and 11(f)). SEM analyses were used to further confirm the removal of the cells

at the luminal surface and demonstrated that decellularized arteries retain the basic extracellular microstructure (Figures 11(g) and 11(h)).

7. Conclusions

In order to provide quality criteria for natural and bio-engineered arteries, different traction mechanical tests have been carried out for two types of blood vessels, native and decellularized. The mechanical properties have been analyzed which are the UTS, Young's modulus, maximum load at failure, and burst pressure. To assess these parameters, several intermediate physical measurements of the vessel samples have been measured such as radial stress, radius, thickness, width, and length. The stress-strain curves are also computed based on an image cross-correlation algorithm developed in-house, combined with a laboratory-prototyped tensile testing machine designed for this purpose.

Strain at failure is seen to increase after decellularization due to cell removal and increased collagen fiber mobility along with the uncrimping of collagen fibers. After decellularization the collagen matrix remains, but other cellular proteins are removed. Therefore, the amount of collagen tends to increase as a percentage of dry weight after decellularization. Then, the increase in stiffness in terms of elastic modulus in the decellularized arteries may be due to the decrease in the cell layer, leaving only a hardening collagen layer (shown in Figure 11). Note that the results are interesting for future experiments or biomedical applications in which different coatings are tested to reinforce the strength of the arteries.

Several studies have shown structural alterations that could be related to changes in mechanical properties. Though the intention of most decellularization procedures is to effectively remove all the cells and nuclear components while minimize disruption to the ECM, the removal of cells can lead to changes to native ECM structure [29]. Moreover, depending on the decellularization method some studies have demonstrated alterations of the ECM structure and thus in the mechanical properties, being SDS and Triton X-100 based protocols more suitable for maintaining the major structure of the elastin and collagen network in the ECM [34].

In summary, this technique is able to measure the strain in the regime of large displacements and enables high-resolution image of the local strains. Thus, it provides a valuable tool for characterizing several biomechanical parameters of the vessels (Young's modulus, stress-strain curve, etc.) and also other hyperelastic materials through uniaxial (or biaxial) tension test. Finally, it is worth pointing out that with image cross-correlation algorithm it is possible to obtain a two-dimensional strain map, from which the heterogeneity and several components of the strain tensor can be reconstructed from a single measurement. In this way, it provides a 2D tracking of the mechanical properties variations; hence a deeper insight of the stress test is obtained.

Data Availability

The data used to support the findings of this study are available from the corresponding author upon request.

Conflicts of Interest

The authors declare that there are no conflicts of interest regarding the publication of this paper.

Acknowledgments

Supplementary Materials

Visualization 1: tracking algorithm for uniaxial tensile test until failure applied in an artery. Green dots represent the center of each block in the discretized ROI and the green line represents the movement apropos of the first frame of the recorded sequence. A pause of 20 seconds has been set between the acquisitions of consecutive frames. *(Supplementary Materials)*

References

[1] C. Quint, Y. Kondo, R. J. Manson, J. H. Lawson, A. Dardik, and L. E. Niklason, "Decellularized tissue-engineered blood vessel as an arterial conduit," *Proceedings of the National Acadamy of Sciences of the United States of America*, vol. 108, no. 22, pp. 9214–9219, 2011.

[2] E. López-Ruiz, S. Venkateswaran, M. Perán et al., "Poly(ethylmethacrylate-co-diethylaminoethyl acrylate) coating improves endothelial re-population, bio-mechanical and anti-thrombogenic properties of decellularized carotid arteries for blood vessel replacement," *Scientific Reports*, vol. 7, no. 1, 2017.

[3] A. Carpentier, J. L. Guermonprez, A. Deloche, C. Frechette, and C. DuBost, "The aorta-to-coronary radial artery bypass graft: a technique avoiding pathological changes in grafts," *The Annals of Thoracic Surgery*, vol. 16, no. 2, pp. 111–121, 1973.

[4] L. R. Caplan, "Lacunar infarction and small vessel disease: pathology and pathophysiology," *Journal of Stroke*, vol. 17, no. 1, p. 2, 2015.

[5] F. M. van der Valk, S. L. Verweij, K. A. Zwinderman et al., "Thresholds for arterial wall inflammation quantified by 18F-FDG PET imaging," *JACC: Cardiovascular Imaging*, vol. 9, no. 10, pp. 1198–1207, 2016.

[6] L. Iop and G. Gerosa, "Guided tissue regeneration in heart valve replacement: from preclinical research to first-in-human trials," *BioMed Research International*, vol. 2015, Article ID 432901, 13 pages, 2015.

[7] A. Keable, K. Fenna, H. M. Yuen et al., "Deposition of amyloid β in the walls of human leptomeningeal arteries in relation to perivascular drainage pathways in cerebral amyloid angiopathy," *Biochimica et Biophysica Acta (BBA) - Molecular Basis of Disease*, vol. 1862, no. 5, pp. 1037–1046, 2016.

[8] S. L. Dahl, C. Rhim, Y. C. Song, and L. E. Niklason, "Mechanical properties and compositions of tissue engineered and native

arteries," *Annals of Biomedical Engineering*, vol. 35, no. 3, pp. 348–355, 2007.

[9] Y. Zhao, S. Zhang, J. Zhou et al., "The development of a tissue-engineered artery using decellularized scaffold and autologous ovine mesenchymal stem cells," *Biomaterials*, vol. 31, no. 2, pp. 296–307, 2010.

[10] Y. M. Ju, J. S. Choi, A. Atala, J. J. Yoo, and S. J. Lee, "Bilayered scaffold for engineering cellularized blood vessels," *Biomaterials*, vol. 31, no. 15, pp. 4313–4321, 2010.

[11] W. Gong, D. Lei, S. Li et al., "Hybrid small-diameter vascular grafts: Anti-expansion effect of electrospun poly ε-caprolactone on heparin-coated decellularized matrices," *Biomaterials*, vol. 76, pp. 359–370, 2016.

[12] Y.-C. Fung, *Biomechanics*, Springer, 1990.

[13] J. D. Enderle and J. D. Bronzino, *Introduction to Biomedical Engineering*, Academic Press, 2012.

[14] F. A. Duck, *Physical Properties of Tissues: A Comprehensive Reference Book*, Academic Press, 2013.

[15] A. N. Natali, E. L. Carniel, P. G. Pavan, P. Dario, and I. Izzo, "Hyperelastic models for the analysis of soft tissue mechanics: definition of constitutive parameters," in *Proceedings of the Biomedical Robotics and Biomechatronics, BioRob 2006*, pp. 188–191, IEEE, 2006.

[16] E. J. Weinberg and M. R. Kaazempur-Mofrad, "A large-strain finite element formulation for biological tissues with application to mitral valve leaflet tissue mechanics," *Journal of Biomechanics*, vol. 39, no. 8, pp. 1557–1561, 2006.

[17] J. M. Deneweth, S. G. McLean, and E. M. Arruda, "Evaluation of hyperelastic models for the non-linear and non-uniform high strain-rate mechanics of tibial cartilage," *Journal of Biomechanics*, vol. 46, no. 10, pp. 1604–1610, 2013.

[18] G. A. Holzapfel, T. C. Gasser, and R. W. Ogden, "A new constitutive framework for arterial wall mechanics and a comparative study of material models," *Journal of Elasticity*, vol. 61, no. 1–3, pp. 1–48, 2000.

[19] G. A. Holzapfel, "Determination of material models for arterial walls from uniaxial extension tests and histological structure," *Journal of Theoretical Biology*, vol. 238, no. 2, pp. 290–302, 2006.

[20] G. A. Holzapfel and R. W. Ogden, "Constitutive modelling of arteries," *Proceedings of the Royal Society A Mathematical, Physical and Engineering Sciences*, vol. 466, no. 2118, pp. 1551–1597, 2010.

[21] R. P. Vito and S. A. Dixon, "Blood vessel constitutive models—1995–2002," *Annual Review of Biomedical Engineering*, vol. 5, no. 1, pp. 413–439, 2003.

[22] C. M. García-Herrera, D. J. Celentano, M. A. Cruchaga et al., "Mechanical characterisation of the human thoracic descending aorta: experiments and modelling," *Computer Methods in Biomechanics and Biomedical Engineering*, vol. 15, no. 2, pp. 185–193, 2012.

[23] C. M. García-Herrera, D. J. Celentano, and M. A. Cruchaga, "Bending and pressurisation test of the human aortic arch: experiments, modelling and simulation of a patient-specific case," *Computer Methods in Biomechanics and Biomedical Engineering*, vol. 16, no. 8, pp. 830–839, 2013.

[24] K. Schmidt-Nielsen, *Animal Physiology: Adaptation and Environment*, Cambridge University Press, 1997.

[25] V. Alastrué, E. Peña, M. Martínez, and M. Doblaré, "Experimental study and constitutive modelling of the passive mechanical properties of the ovine infrarenal vena cava tissue," *Journal of Biomechanics*, vol. 41, no. 14, pp. 3038–3045, 2008.

[26] W. Sheridan, G. Duffy, and B. Murphy, "Mechanical characterization of a customized decellularized scaffold for vascular tissue engineering," *Journal of the Mechanical Behavior of Biomedical Materials*, vol. 8, pp. 58–70, 2012.

[27] M. Chow and Y. Zhang, "Changes in the mechanical and biochemical properties of aortic tissue due to cold storage," *Journal of Surgical Research*, vol. 171, no. 2, pp. 434–442, 2011.

[28] B. D. Stemper, N. Yoganandan, M. R. Stineman, T. A. Gennarelli, J. L. Baisden, and F. A. Pintar, "Mechanics of fresh, refrigerated, and frozen arterial tissue," *Journal of Surgical Research*, vol. 139, no. 2, pp. 236–242, 2007.

[29] C. Williams, J. Liao, E. Joyce et al., "Altered structural and mechanical properties in decellularized rabbit carotid arteries," *Acta Biomaterialia*, vol. 5, no. 4, pp. 993–1005, 2009.

[30] G. Jiménez, E. López-Ruiz, W. Kwiatkowski et al., "Activin A/BMP2 chimera AB235 drives efficient redifferentiation of long term cultured autologous chondrocytes," *Scientific Reports*, vol. 5, Article ID 16400, 2015.

[31] M. Jerabek, Z. Major, and R. Lang, "Strain determination of polymeric materials using digital image correlation," *Polymer Testing*, vol. 29, no. 3, pp. 407–416, 2010.

[32] P. Hung and A. S. Voloshin, "In-plane strain measurement by digital image correlation," *Journal of the Brazilian Society of Mechanical Sciences and Engineering*, vol. 25, no. 3, 2003.

[33] R. E. Shadwick, "Mechanical design in arteries," *Journal of Experimental Biology*, vol. 202, no. 23, pp. 3305–3313, 1999.

[34] Y. Zou and Y. Zhang, "Mechanical evaluation of decellularized porcine thoracic aorta," *Journal of Surgical Research*, vol. 175, no. 2, pp. 359–368, 2012.